CORA Cork Open Research Archive
Cartlann Taighde Oscailte Chorcaí

Title	Electronic and optical properties of SixGe1-x-ySny alloys lattice-matched to Ge
Authors	Pearce, Phoebe M.;Broderick, Christopher A.;Nielsen, Michael P.;Johnson, Andrew D.;Ekins-Daukes, Nicholas J.
Publication date	2022-01-18
Original Citation	Pearce, P. M., Broderick, C. A., Nielsen, M. P., Johnson, A. D. and Ekins-Daukes, N. J. (2022) 'Electronic and optical properties of SixGe1-x-ySny alloys lattice-matched to Ge', Physical Review Materials, 6(1), 015402 (15pp). doi: 10.1103/PhysRevMaterials.6.015402
Type of publication	Article (peer-reviewed)
Link to publisher's version	10.1103/PhysRevMaterials.6.015402
Rights	© 2022, American Physical Society. All rights reserved.
Download date	2026-11-04 08:39:41
Item downloaded from	https://hdl.handle.net/10468/13084

UCC
University College Cork, Ireland
Coláiste na hOllscoile Corcaigh

Supplemental Material for "Electronic and optical properties of $Si_xGe_{1-x-y}Sn_y$ alloys lattice-matched to Ge"

Phoebe M. Pearce,[1,*] Christopher A. Broderick,[2,3,†] Michael P. Nielsen,[4] Andrew D. Johnson,[5] and Nicholas J. Ekins-Daukes[1,4]

[1]*Department of Physics, Imperial College London, South Kensington, London SW7 2AZ, United Kingdom*
[2]*Tyndall National Institute, University College Cork, Lee Maltings, Dyke Parade, Cork T12 R5CP, Ireland*
[3]*Department of Physics, University College Cork, Cork T12 YN60, Ireland*
[4]*School of Photovoltaic and Renewable Engineering, University of New South Wales, Sydney, New South Wales 2052, Australia*
[5]*IQE plc., Pascal Close, St. Mellons, Cardiff CF3 0LW, United Kingdom*

(Dated: November 27, 2021)

I. PHOTOREFLECTANCE DATA FITTING

Assuming the anomalous features observed in the PR of the samples (see Fig. S1) are interference fringes due to reflection at the buried InGaAs interface, the period of oscillations of the fringes is determined by the $Si_xGe_{1-x-y}Sn_y$ layer thickness, while the envelope shape of the oscillations depends on the modulation of the refractive index by the pump beam. While Kallergi[1] and Huang[2] attribute the interference to modulation of the refractive index of doped GaAs substrates, rather than modulation of the refractive index of the epi-layer, this explanation is unlikely for the $Si_xGe_{1-x-y}Sn_y$ samples as the thickness of the samples ($\approx 1.8-2$ µm) means that very few (<1%) of the high energy photons from the pump beam (532 nm laser) incident on the sample are able to reach the GaAs substrate (Set A) or InGaAs buffer layer (Set B). However, the model presented in [1] and [2] can be adapted relatively simply to assume modulation of the epilayer refractive index rather than the substrate.

The photoreflectance signal $\Delta R/R$ is the relative change in the reflectivity with and without the pump beam, so $\Delta R/R = (R' - R)/R$ where R' is the modulated reflectivity and R is the unmodulated reflectivity. For instance, for Set A, considering the three layers in the epitaxial structure ($Si_xGe_{1-x-y}Sn_y$, Ge seed layer, and GaAs substrate), the reflectivity is a function of the relevant thicknesses and refractive indices: the unmodulated reflectivity $R(E, n_{SiGeSn}, n_{Ge}, n_{(In)GaAs}, d_{SiGeSn}, d_{Ge})$ and the modulated reflectivity $R'(E, n_{SiGeSn} + \delta n_{SiGeSn}, n_{Ge} + \delta n_{Ge}, n_{GaAs} + \delta n_{GaAs}, d_{SiGeSn}, d_{Ge})$ where the n are the complex refractive indices. Assuming the refractive indices of the Ge and GaAs are not significantly affected since very little pump light is able to reach these layers, the functional dependence of the modulated reflectivity simplifies to $R'(E, n_{SiGeSn} + \delta n_{SiGeSn}, n_{Ge}, n_{GaAs}, d_{SiGeSn}, d_{Ge})$. Because of the presence of the Ge seed layer, the multi-layer reflectivity model is more complex than in [1] and [2], and rather than constructing an analytical expression for the multi-layer interference, Solcore's TMM optical model[3] was used to calculate both R' and R, and thus $\frac{\Delta R}{R}$ with and without modulation of the dielectric function of the . The change in the refractive index was expressed as in [1]:

$$\delta n_{SiGeSn} \propto (n_{SiGeSn}^2 - 1)e^{-\gamma E} \tag{1}$$

The thickness, constant of proportionality A, and γ were fitted to the data (d_{Ge} was kept fixed at 60 nm).

Optical constants for the different compositions were obtained from ellipsometry[4], and these could be used in this model for n_{SiGeSn}. However, this raises an issue, since the location of the critical points which occur in the PR data is what leads to certain values of n and κ; using externally imposed values of n and κ is not consistent with also fitting the location of the critical points. However, it is possible to instead fit the interference fringes and signal from the critical point simultaneously by expressing the optical constants in terms of an analytical model such as the Adachi model[5] and fitting the optical constant modulation using the optical constants calculated directly from these analytical expressions, and the photoreflectance signal to their third derivative.

The real and imaginary parts of the dielectric constant, and thus the refractive index n, are calculated according

TABLE S1: All parameters used in fitting the photoreflectance data to a model incorporating both the critical point feature and the effects of thin-film interference in the layer. The ticks in the final two columns indicate whether the parameter affects the fit of the interference fringes, the critical point feature, or both.

Parameter	Description	Interference fringes	PR signal due to CP
E_0	E_0 CP ($\Gamma \rightarrow \Gamma$) centre energy	✓	✓
Δ_0	Split-off hole energy	✓	✓
A_0	Strength of the E_0 transition	✓	
Γ_{0/Δ_0}	Broadening of the E_0 transition	✓	✓
γ	Exponent for envelope	✓	
A_n	Strength of n modulation	✓	
$A_{CP,0}$	Strength of E_0 CP signal		✓
Φ_{0/Δ_0}	Phase of E_0 and $E_0 + \Delta_0$ CP signal		✓
A_{CP,Δ_0}	Strength of $E_0 + \Delta_0$ CP signal		✓
E_{ex}	E_0 exciton binding energy transition energy		✓
A_{ex}	Strength of the exciton PR signal		✓
Γ_{ex}	Broadening of the exciton PR signal		✓
Φ_{ex}	Phase of the exciton PR signal		✓
d_{SiGeSn}	Thickness of the layer	✓	
d_{GaAs}	Thickness of the GaAs layer (Set B only)	✓	
Φ_{PR}	Overall phase of the PR measurement	✓	✓
C	Constant offset of measurement	✓	✓

to:[5]

$$\begin{aligned}
&\varepsilon = AE_0^{-1.5}\left\{f(\chi_0) + \tfrac{1}{2}\left(\tfrac{E_0}{E_0+\Delta_0}\right)^{1.5} f(\chi_{\mathrm{so}})\right\} \\
&f(\chi_0) = \chi_0^{-2}\left[2 - (1+\chi_0)^{0.5} - (1-\chi_0)^{0.5}\right] \\
&f(\chi_{\mathrm{so}}) = \chi_{\mathrm{so}}^{-2}\left[2 - (1+\chi_{\mathrm{so}})^{0.5} - (1-\chi_{\mathrm{so}})^{0.5}\right] \\
&\chi_0 = \tfrac{\hbar\omega + i\Gamma_{0/\Delta_0}}{E_0} \\
&\chi_{\mathrm{so}} = \tfrac{\hbar\omega + i\Gamma_{0/\Delta_0}}{E_0+\Delta_0} \\
&n = \Re\{\sqrt{\varepsilon}\}
\end{aligned} \tag{2}$$

The change in the refractive index of due to modulation by the pump beam is given by (using the n from eq. 2):

$$\begin{aligned}
&\delta_n = A_n e^{\gamma E}\left(n^2 - 1\right) \\
&\tilde{n} = n + \delta n
\end{aligned} \tag{3}$$

This modulated refractive index is fed into the TMM model of the layer stack to calculate R'; R is similarly calculated with the unmodulated refractive index n, so that the change in reflectivity $\Delta R = R' - R$ due to interference can be calculated. The interference signal IS is given by $(R' - R)/R$.

The critical point feature in the photoreflectance data is fitted using:

$$CP = \Re\left[\frac{A_{CP,0}e^{i\Phi_0}}{(E - E_0 + i\Gamma_{0/\Delta_0})^{5/2}} + \frac{A_{ex}e^{i\Phi_{ex}}}{(E - E_{ex} + i\Gamma_{ex})^2} + \frac{A_{CP,\Delta_0}e^{i\Phi_{\Delta_0}}}{(E - (E_0+\Delta_0) + i\Gamma_{\Delta_0})^{5/2}}\right] \tag{4}$$

Finally, the overall modelled value for the PR signal is the sum of the contributions, plus a constant offset. In addition, a phase factor is fitted (this is due to the phase chosen for the lock-in amplifier during the measurement):

$$\frac{\Delta R}{R} = \Re\{(CP + IS + C)e^{i\Phi_{PR}}\} \tag{5}$$

The symbols used for each parameter, and their physical meaning, are given in Table S1.

This model, which fits the full photoreflectance signal, has a large number of parameters to account for the layer thicknesses, peak strength and broadening, phase factors, and degree of optical constant modulation. The differential evolution (DE) optimization technique was used to fit the model to the data for all nine samples. Since the model has a large number of parameters, the differential evolution was run multiple times for each sample to identify whether consistent results could be obtained between runs of the optimization algorithm. The fits with the lowest root mean

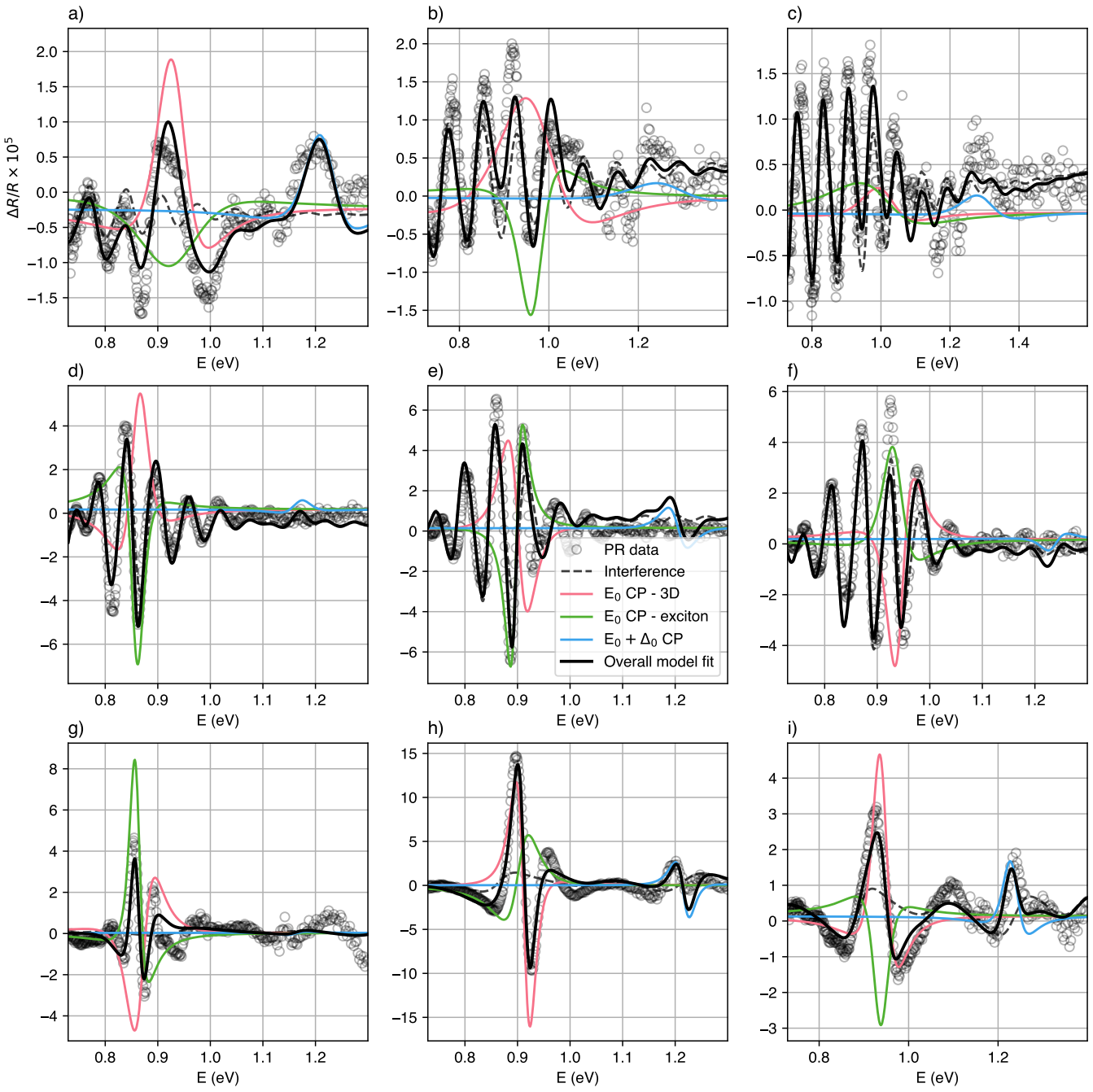


FIG. S1: Best fits (out of 10 runs of the differential evolution model fitting) to the PR data of the samples from a)-c) Set A, from lowest to highest compositio; d)-f) $\sim$ 2 µm Set B samples from lowest to highest composition; and g)-i) $\sim$ 400 nm Set B samples from lowest to highest composition, using the combined interference/critical point model. The overall model fit (black line) is shown in addition to contributions from thin-film interference, the E_0 critical point (plus excitonic contribution) and the $E_0 + \Delta_0$ critical point.

square error (RMSE) are shown in Fig. S1. A list of all fitted parameters fitted and the bounds imposed is given in Table S2. This shows that while the standard deviation across 10 iterations of the model fitting procedure was large for some parameters, the error associated with the key parameters E_0 and Δ_0 was relatively small.

As the Set B samples were grown after the Set A samples, when the effect of interference of the PR signal had been identified, two versions of each composition were grown; $\sim$ 2 µm samples, similar to the Set A samples, and thinner $\sim$ 400 nm layers were grown as part of Set B. The expectation was that for the thinner samples, the interference

fringes would be significantly wider, and the photoreflectance signal arising from the critical points would be more easily identifiable; this can be seen clearly in the data in Fig. S1(g)-(i). The two different thicknesses of Set B samples were fitted independently, but the values for E_0 and Δ_0 are in good agreement for each composition, validating the model presented here for simultaneous fitting of the critical points and interference fringes, and the consistency of the composition grown across two different sample thicknesses.

TABLE S2: Full results of fits to the photoreflectance data using the combined thin-film interference and critical point model. The meaning of the parameters is given in Table S1. The fit is run 10 times for each sample; the values given are the mean result across the 10 fitting runs, with the standard deviation given in brackets.

Sample	$\mathbf{A_0}$	$\mathbf{E_0}$ (eV)	$\mathbf{\Gamma_0}$ (eV)	$\mathbf{\Delta_0}$ (eV)	$\mathbf{A_{CP,0}}$ $\times 10^8$	$\mathbf{\Phi_{0/\Delta_0}}$ (rad)	$\mathbf{A_{CP,\Delta_0}}$ $\times 10^9$	$\mathbf{A_{ex}}$ $\times 10^8$	$\mathbf{E_{ex}}$ (meV)	$\mathbf{\Phi_{ex}}$ (rad)	$\mathbf{d_{SiGeSn}}$ (nm)	$\mathbf{d_{GaAs}}$ (nm)	γ (eV^{-1})	$\mathbf{A_n}$ $\times 10^6$	$\mathbf{\Phi_{PR}}$ (rad)
A1	3.1 (0.4)	0.94 (0.007)	0.065 (0.003)	0.284 (0.01)	2.0 (0.5)	-1.6 (0.3)	14.5 (4.0)	8.6 (0.8)	5 (2)	0.4 (0.3)	1811 (41)	n/a	1.2 (0.2)	0.08 (0.01)	-1.3 (1.2)
A2	3.7 (0.3)	1.001 (0.024)	0.142 (0.004)	0.273 (0.02)	9.1 (0.6)	-1.2 (0.5)	25.5 (14.0)	3.9 (1.0)	6 (2)	1.2 (0.7)	1746 (6)	n/a	1.8 (0.1)	0.09 (0.01)	-0.1 (0.2)
A3	3.9 (0.0)	1.014 (0.002)	0.112 (0.006)	0.294 (0.01)	1.1 (0.2)	-1.9 (0.3)	19.8 (5.0)	9.3 (0.5)	6 (2)	-2.3 (0.1)	1828 (2)	n/a	1.6 (0.1)	0.09 (0.01)	-0.1 (0.2)
B1 - thin	1.9 (0.5)	0.866 (0.007)	0.037 (0.002)	0.291 (0.01)	1.5 (0.4)	1.1 (1.5)	3.4 (2.0)	3.9 (1.6)	6 (3)	-0.6 (2.0)	332 (11)	503 (16)	0.5 (0.4)	2.18 (1.08)	-0.3 (1.5)
B1 - thick	3.1 (0.4)	0.866 (0.003)	0.037 (0.002)	0.29 (0.01)	1.3 (0.3)	-2.5 (0.2)	1.8 (2.0)	4.3 (1.0)	5 (1)	-0.4 (0.2)	2073 (16)	504 (4)	0.4 (0.3)	1.48 (0.48)	2.3 (0.1)
B2 - thin	2.9 (0.4)	0.911 (0.003)	0.027 (0.001)	0.301 (0.01)	2.0 (0.2)	-0.8 (0.3)	4.4 (2.0)	7.9 (1.4)	6 (2)	1.7 (0.4)	362 (8)	502 (15)	0.4 (0.3)	2.28 (1.31)	-0.4 (1.3)
B2 - thick	3.1 (0.4)	0.907 (0.015)	0.036 (0.002)	0.292 (0.01)	1.4 (0.1)	-0.3 (1.5)	4.1 (2.0)	4.6 (1.8)	7 (2)	-0.1 (1.8)	2017 (39)	506 (8)	0.7 (0.4)	4.43 (1.85)	1.5 (0.2)
B3 - thin	2.6 (0.6)	0.953 (0.012)	0.039 (0.001)	0.292 (0.01)	1.4 (0.4)	-1.4 (0.6)	7.0 (1.0)	3.3 (1.4)	7 (2)	-0.0 (0.5)	353 (7)	515 (9)	0.4 (0.3)	2.45 (1.04)	0.2 (1.4)
B3 - thick	3.6 (0.3)	0.949 (0.008)	0.035 (0.003)	0.295 (0.01)	1.3 (0.3)	1.9 (0.6)	3.2 (2.0)	4.6 (2.0)	6 (2)	-1.6 (1.7)	2036 (49)	497 (11)	0.8 (0.5)	3.67 (2.22)	1.5 (0.2)

II. POWER-DEPENDENT PHOTOLUMINESCENCE MEASUREMENTS

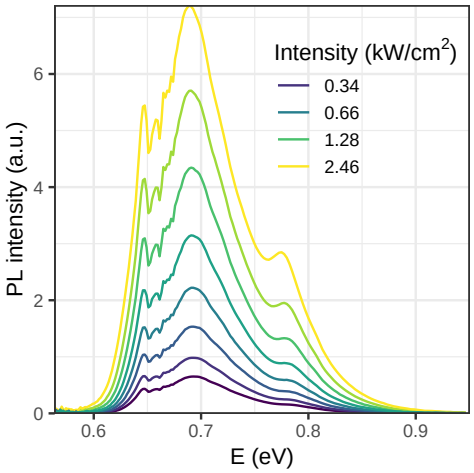


FIG. S2: Measured power-dependent room temperature PL spectra of a reference Ge substrate sample. The incident laser intensity varies from 0.34 kW cm^{-2} (dark purple) to 2.46 kW cm^{-2} (yellow). In addition to the fundamental (indirect Γ-L) band gap emission at 0.69 eV, satellite features related to additional phonon-assisted emission processes are also visible.

Unnormalised power-dependent room-temperature PL measurements of the Ge and samples are shown in Fig. S2 and S3 respectively. The power dependence of the integrated PL intensity for each sample is shown in Fig. S4.

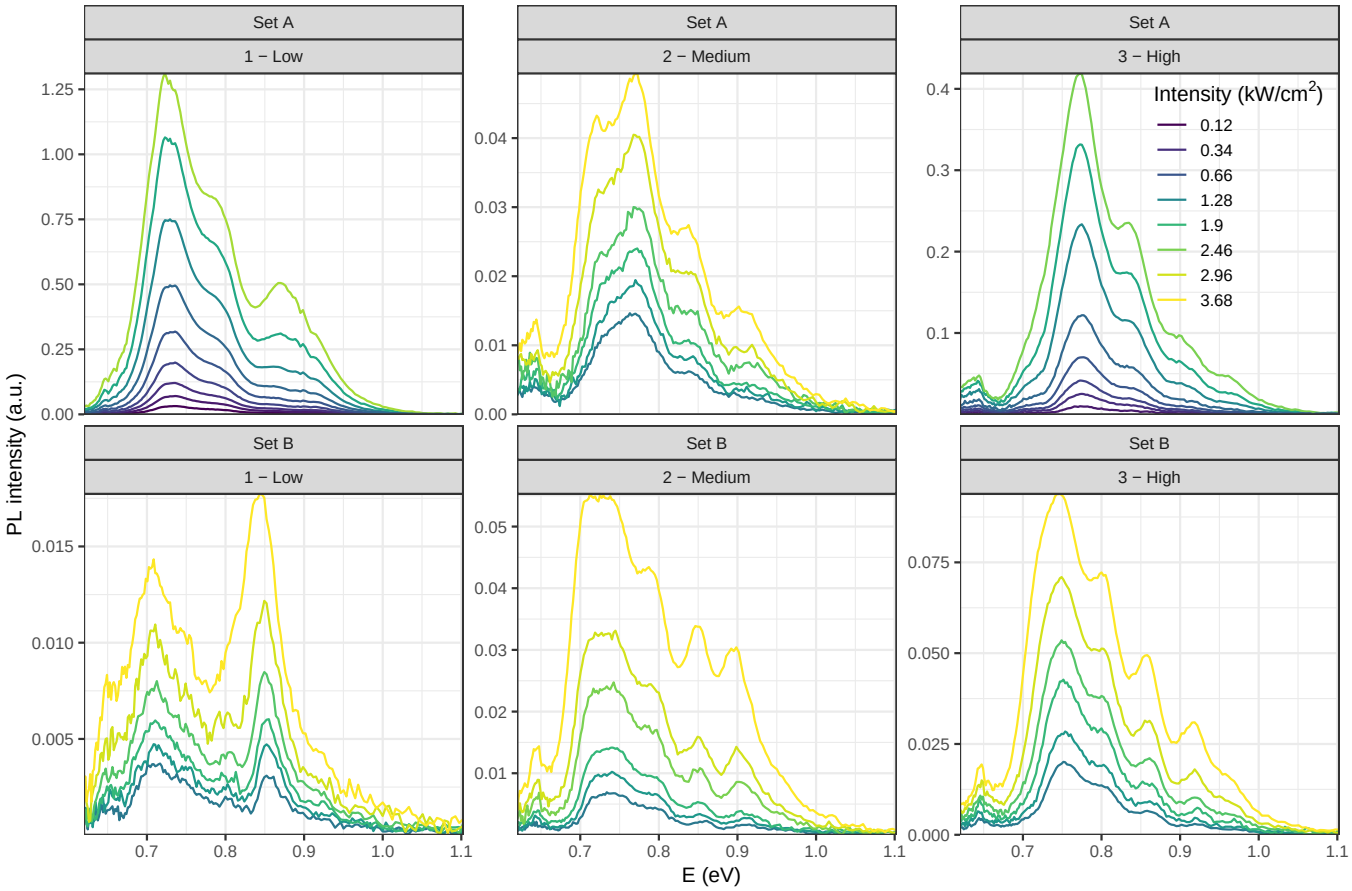


FIG. S3: Measured power-dependent room temperature PL spectra of the samples. Measurements for sample set B were performed on "thick" samples (≈ 2 µm). Samples A1 and A3 had higher PL intensities at a given incident laser intensity than the other four samples, so PL measurements performed for incident laser intensities between 0.12 and 2.46 kW cm^{-2}. PL measurements for the other four samples were performed for incident laser intensities between 1.23 and 3.68 kW cm^{-2}.

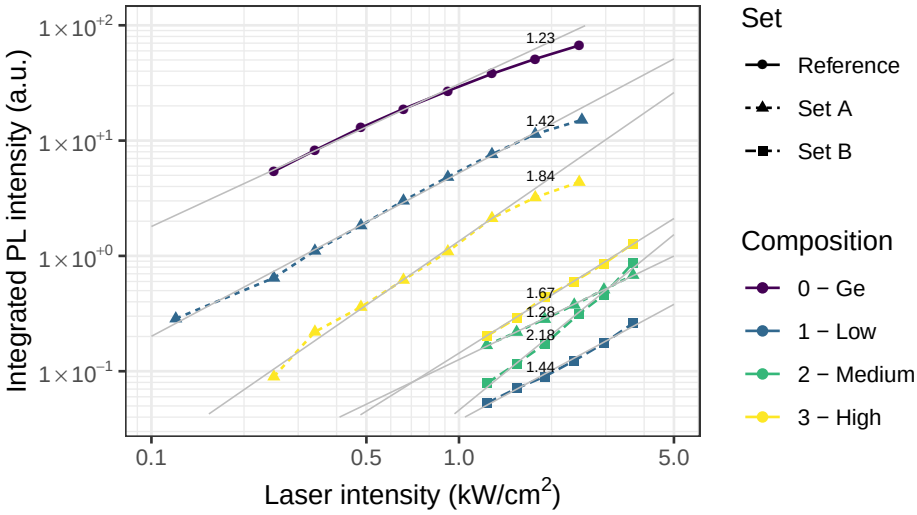


FIG. S4: Variation of integrated room-temperature PL intensity over the whole measurement range (0.62 eV to 1.10 eV/1125 nm to 2000 nm) with incident laser intensity for each sample. The grey lines show fits to a power law (eq. 11); the number by each line is the fitted value of m. For the higher PL intensity samples (Ge, A1 and A3), only data for powers up to and including 0.66 kW/cm^2 was included as the dependence above these powers becomes visibly sub-linear on the log-log plot.

III. LOCAL SAMPLE HEATING DUE TO LASER EXPOSURE

To estimate the temperature increase due to the high-power laser (up to 3W total power, or 3.68 kW/cm^2 intensity, for some samples) used for the PL measurements, two methods were used: fitting the slope of the high-energy edge of the measured PL to find the carrier temperature, and solving the steady-state heat diffusion equation.

A. Obtaining the lattice temperature from PL data

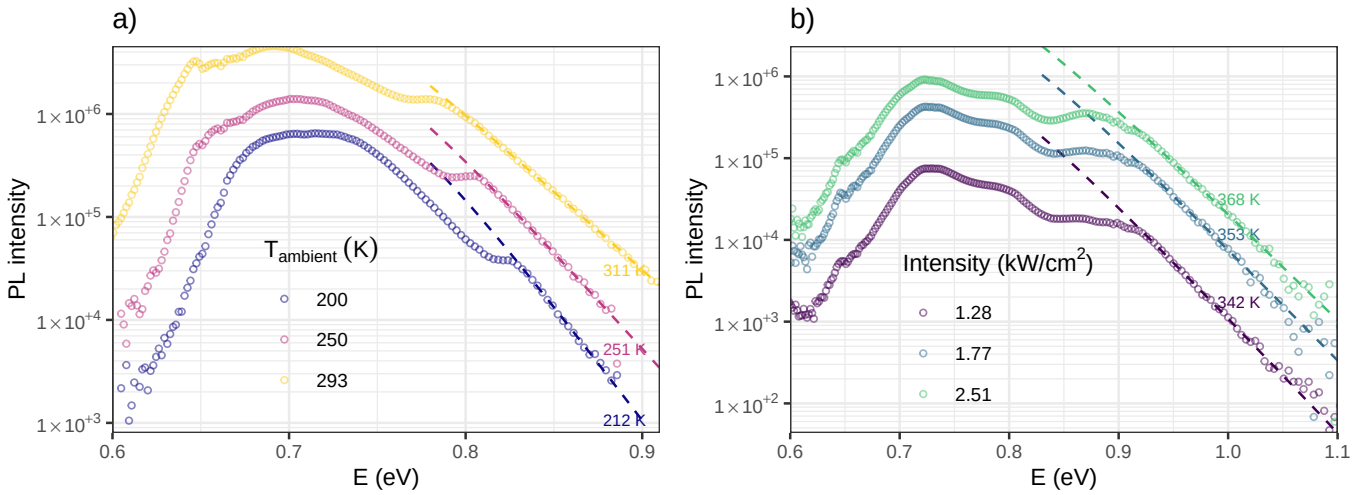


FIG. S5: Fits of the high-energy PL edge to eq. 6. a) Shows data for Ge, measured at varying temperatures (in a cryostat) with 1 W (1.28 kW/cm^2) of incident laser power (intensity). b) Shows data for $Si_xGe_{1-x-y}Sn_y$ sample A1, all measured at room temperature (not using a cryostat) but with laser power (intensity) between 1 W (1.28 kW/cm^2) and 3 W (2.51 kW/cm^2). In both plots, the labels next to the lines indicate the temperature obtained from fitting eq. 6. The spectra are rigidly shifted along the y-axis for clarity.

Following the method applied to Ge by Lieten et al.[6], we fit the high-energy edge of the measured PL using:

$$I_{PL} \propto (E - E_0)^{0.5}\, e^{-(E-E_0)/kT_c} \tag{6}$$

The first term approximates the density of states above the bandgap, and the second term is a Boltzmann distribution where T_c is the carrier temperature. Figure S5a shows the results of fitting this equation to data for a Ge reference sample measured at different temperatures using a laser power of 1 W. Below room temperature (200K and 250K), the measurements were carried out in a cryostat (i.e. the sample is actively being cooled), and the fitted T_c values deviate by 12K and 1K from the nominal temperature. At room temperature (293K), no cryostat was used, and the T_c fitted is 18K above room temperature. Fitting the high-energy PL edge in this manner thus gives reasonable results for the Ge reference sample. In Fig. S5b, PL of $Si_xGe_{1-x-y}Sn_y$ sample A1 measured at room temperature (without a cryostat) at different lasers powers above 1W (1.28 kW/cm^2) is shown. Fitting the high-energy slope here gives T_c values between 49K (1W laser power) and 60K (3W laser power) above room temperature, indicating there is quite significant heating of the samples due to laser exposure.

B. Calculating the temperature due to laser exposure

The steady-state (i.e. time-invariant) heat equation is:

$$k\, \nabla^2 T = \dot{q} \tag{7}$$

Where k is the conductivity of Ge (material constants for Ge are used throughout as an estimate for the values), taken to be 0.58 W m^{-1} K^{-1}, and $\dot{q}$ is the heat generated in the sample by the laser. In this case, we assume a

Gaussian beam profile and Beer-Lambert absorption of the laser in the sample, and thus the problem can be reduced to two dimensions:

$$k\left(\frac{\partial^2 T^2}{\partial x^2}+\frac{\partial^2 T^2}{\partial y^2}\right)=\frac{2P(1-R)\alpha}{\pi r_s^2}e^{-2(y-y_{inc})^2/r_s^2}e^{-\alpha x} \tag{8}$$

Where P is the total incident laser power, as measured, R is the fraction of light reflected at the front surface (calculated to be 0.52 for Ge at 532 nm), α is the absorption coefficient of Ge at 532 nm (5.5×10^4), and r_s is the radius of the laser spot size where its intensity falls to $1/e^2$ of the maximum intensity. It was assumed that the material properties (conductivity and absorption coefficient) are constant. Integrating over y and x gives a total absorbed laser power of $P(1-R)$, as required.

To solve this partial differential equation (PDE), we use Firedrake[7], which uses the Finite Element Method (FEM) to numerically solve PDEs (which can be expressed symbolically). The boundary conditions used assume that no heat can flow across the surfaces of the sample in contact with air (i.e. the front surface, where the laser is incident, and the sides) so that $\nabla u\cdot\vec{n}=0$ where $\vec{n}$ is the unit vector pointing out of the surface. The rear surface allows heat flow and is maintained at the ambient temperature; the rear surface of the sample is in contact with a copper plate, which is much larger than the sample itself, and it is assumed that heat is conducted away from the sample efficiently by the copper. The thickness of the sample was fixed at 500 µm, and the width at 2.5 mm. The samples measured have variable thickness depending on the substrate used, and differ in width as samples for measurement were cleaved manually, but these values are representative for the whole sample set.

Results of the FEM calculations are shown in Fig. S6. Fig. S6a shows the maximum local temperature and the mean temperature within the radius of the laser spot found in at the sample surface at each incident laser power, while Fig. S6b shows the spatial distribution of temperatures in the sample with 3W incident laser power. These results show that at high laser powers, there is expected to be significant heating of the sample in the area exposed to the laser, up to 100 K for the highest laser power used (3W). The maximum and mean temperatures observed at the sample surface scale linearly with the laser power. We expect these temperatures to be an overestimate as they ignore heat loss through radiation and convection.

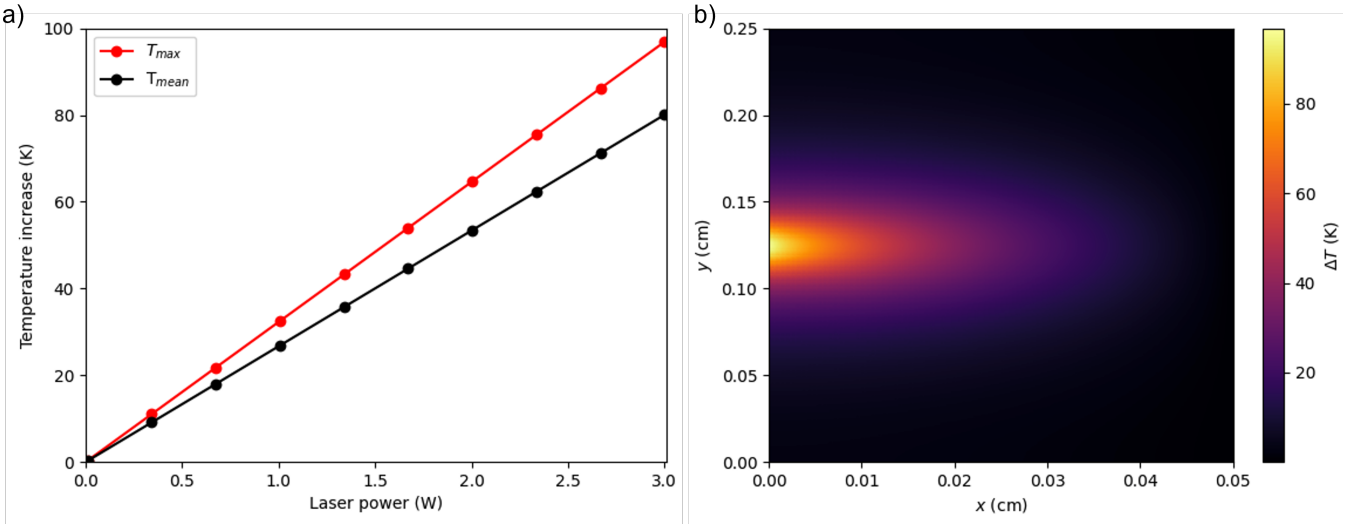


FIG. S6: a) Maximum (T_{max}) and mean (T_{mean}) temperatures observed at the surface of the sample ($x=0$) within the laser spot radius r_s vs. incident laser power. b) Temperature increase (relative to room temperature) for the maximum incident laser power used (3 W). The laser is incident from the left at $x=0$ cm, $y=0.125$ cm

The two methods for calculating the heat generated in the sample by the laser agree quite well; solving the heat equation gave a temperature increase above room temperature of around 25–30K at 1W laser power, and 50–60K at 2W. Looking at Fig. S5b, the carrier temperature fitted to eq. 6 for 1W and 2W incident laser power are 342K and 368K respectively. Taking room temperature to be 293K (20°C), this gives temperature increases of 49K and 75K respectively.

IV. PHOTOLUMINESCENCE DATA FITTING

The Gaussian and Lorentzian peaks fitted to the PL data were expressed as:

$$I_G(E) = \frac{A}{\sigma\sqrt{2\pi}} e^{-\frac{1}{2}\left(\frac{E-E_i}{\sigma}\right)^2} \tag{9}$$

$$I_L(E) = \frac{A\gamma}{\pi} \frac{1}{\left(E-E_i\right)^2 + \gamma^2} \tag{10}$$

The parameters fitted in each case were the centre energy of the peak (E_i), the broadening (standard deviation σ for the Gaussian distributions and scale parameter γ for the Lorentzian distribution), and the strength A, which corresponds to the area under the peak. Figure S7 shows the resulting fits at the highest and lowest incident laser power used to measure each sample. In each case, it was possible to fit the same number and type of peak consistently across data for different incident powers, although for sample A2 it was not possible to fit the two lowest-energy peaks at low power. Figures S8 and S9 show how the centre energies fitted for each peak change with the laser power used; this shows that despite the expected increase in temperature due to the laser, the centre energies fitted are quite constant, although there is some evidence of a general redshift with increasing power for the samples measured at the highest powers (A2, B1, B2 and B3). To avoid issues due to sample heating and band-filling as much as possible, data for the lowest power possible was used to estimate the band gap as presented in Table II of the main manuscript.

The data in Fig. S3 shows that a peak at 0.645 eV/1922 nm is present for all $Si_xGe_{1-x-y}Sn_y$ samples, independent of the laser power used to excite the samples. It is not clearly visible in all the plots in S3 due to the varying intensity of the PL. Since this peak was present for all measurements, it was attributed to some background signal (note that it was not possible to see this peak in the measurements for Ge – there is significant PL intensity from the Ge samples at 0.645 eV, and the PL signal is around 2 orders of magnitude higher than for the samples where this constant-energy peak is apparent, see Figs S2 and S3). This peak did not have the expected power dependence for PL for a bulk material as observed for the other peaks; for instance, sample B3 has around 5 times the PL intensity of sample B1 at a given power (Fig. S3), yet the peaks around 0.645 eV are only around twice as intense, indicating that their source is some external source of background signal with constant intensity (with the remaining difference of intensity being due to the low-energy tail of the PL signal). For this reason, only data above 0.68 eV was used in fitting the PL signal of the samples with relatively low PL intensity (A2, B1, B2 and B3).

Figure S4 shows the variation of the integrated PL intensity (area under the curve) for all samples, integrated over the whole measurement range (0.62 eV to 1.10 eV/1125 nm to 2000 nm). The room temperature power dependence of the integrated PL intensity of all samples follow a power law of the form:

$$I_{PL} \propto I_{laser}^m \tag{11}$$

where I_{PL} is the integrated intensity of the PL signal and I_{laser} is the incident laser intensity (the peak intensity follows a similar power law behaviour for all samples) and m is a positive constant. The samples which showed higher PL intensities (Ge, A1 and A3) become sub-linear on a log-log plot at powers above ≈ 1 kW/cm^2, indicating that at higher powers there may be additional effects such as band-filling which affect the PL intensity. The power law fits shown in Fig. S4 are fitted to data for all the incident intensities for the lower-intensity samples (A2, B1, B2 and B3) and up to and including the measurements at 0.66 kW/cm^2 for the higher-intensity samples (Ge, A1 and A3).

TABLE S3: Power law exponents fitted to the peak and integrated intensity of PL data for Ge and samples.

Sample	m_{int}	m_{peak}
Ge	1.23	1.20
A1	1.42	1.39
A2	1.28	1.11
A3	1.83	1.84
B1	1.43	1.53
B2	2.17	1.88
B3	1.67	1.38

While PL from all the samples follows a power law as expected, the variation of the exponent m between samples does not seem to correlate to an obvious parameter such as peak energy, composition or Si:Sn ratio, and lies between

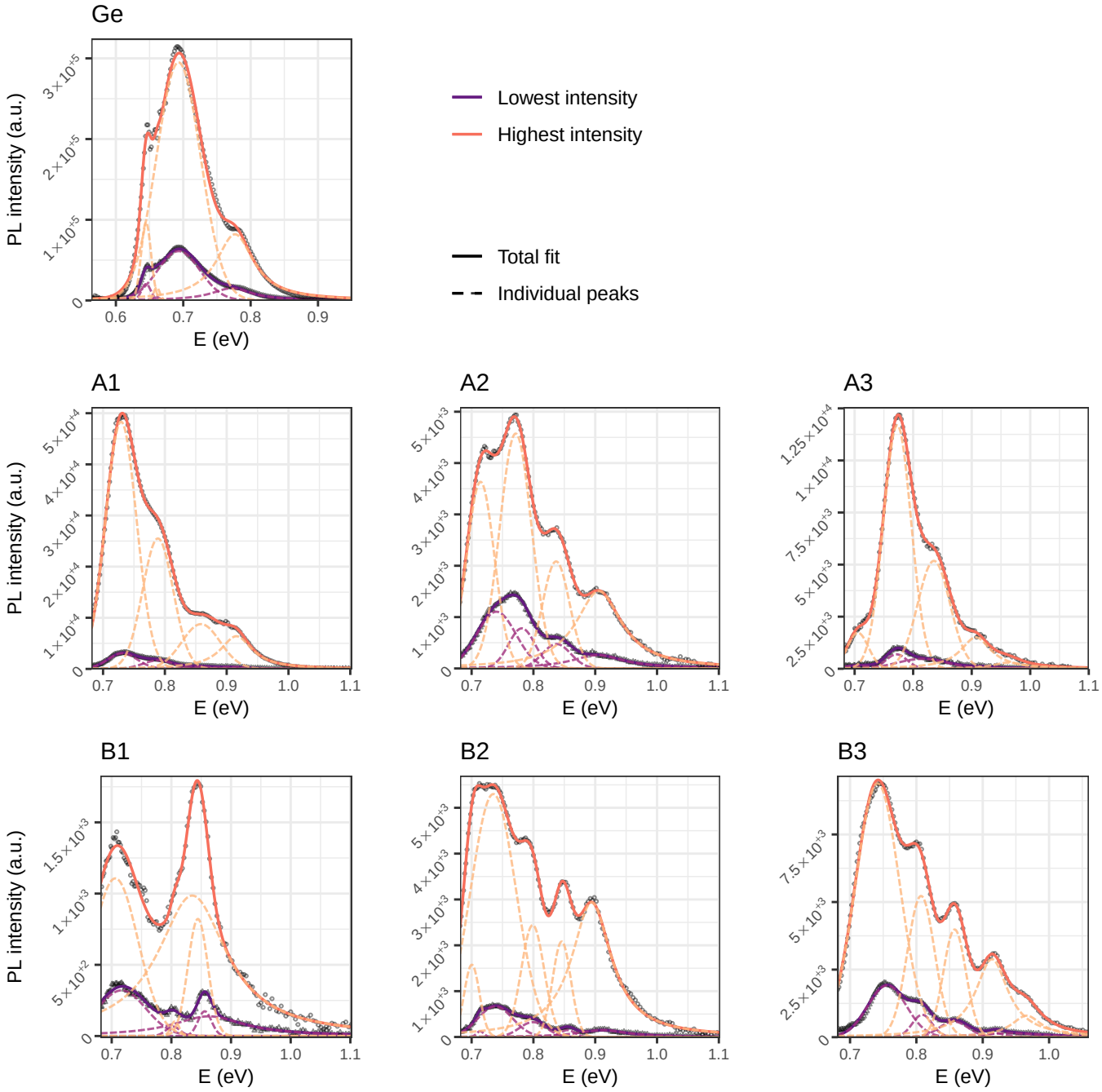


FIG. S7: Fits to power-dependent room-temperature PL data using Gaussian and Lorentzian lineshapes. The lowest and highest power measured and the corresponding fits (total fit and individual peaks) are shown for each sample.

1 and 2 for all the samples. The Ge substrate has an exponent of 1.23, which differs from values previously reported in the literature as summarized in Table S4; Lieten et al.[6] report a power law exponent of 2.02, relating to PL from the indirect transition, while Klingenstein & Schweizer[8] report an exponent of 1 for the indirect transition and 1.6 for the direct transition, with the latter measured at significantly higher laser intensities by around two orders of magnitude (Table S4). Both of these sets of measurements were taken at low temperature (9K and 2K respectively). Measurements of the Ge sample at 30 K give an exponent of 1.66, higher than the room-temperature value of 1.23. The laser intensity used here for the low-temperature measurements is between those used by Lieten et al. and Klingenstein & Schweizer, and an intermediate value of the power law exponent is obtained. Considering the power-dependent data for Ge at room temperature shown here, and the exponents for the indirect transition obtained by

TABLE S4: Summary of some parameters from this and previous work on Ge photoluminescence.

Reference	Power law exponent	Power densities	Temperature (K)
Lieten et al.[6]	2.02 (indirect)	0.008–0.128 kW/cm^2	9
Klingenstein & Schweizer[8]	1 (indirect), 1.6 (direct)	0.8–6.7 kW/cm^2	2
van Driel et al.[9]	not reported	0.05–10^5 kW/cm^2	174, 295
This work - 295 K	1.23 (indirect)	0.12–3.68 kW/cm^2	295
This work - 30 K	1.68 (indirect)	0.01–0.25 kW/cm^2	30

Lieten at low laser intensity and by Klingenstein at high power, it appears that higher incident laser power decreases the exponent m while higher temperatures lead to higher m. This indicates that the behaviour of the Ge PL is quite consistent with that previously observed once variations of the exponent m with temperature and incident laser intensity are taken into account.

Schmidt et al.[10] formulated a general model to describe the dependence of the intensity of the near-bandgap luminescence on the incident laser power by considering rate equations for carrier excitation and different recombination processes, including free and bound excitons and recombination involving donors and acceptors, and non-radiative processes; this model indicates that a value of m between 1 and 2 is consistent with interband radiative recombination, rather than transitions involving bound states (such as would occur with defects), indicating that the PL emitted by the Ge and samples at room temperature is consistent with radiative recombination in the bulk.

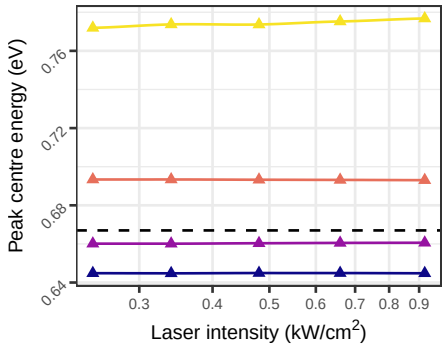


FIG. S8: Dependence of fitted peak centre energy on incident laser intensity for Ge.

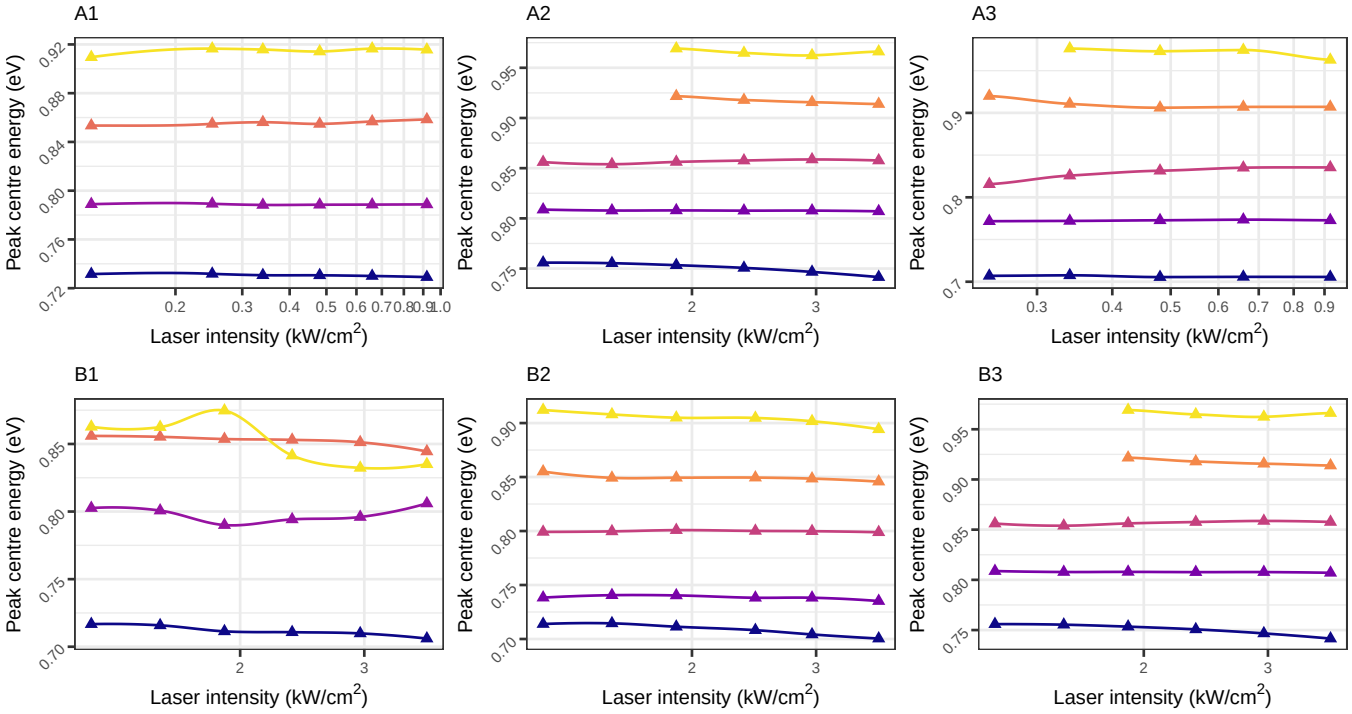


FIG. S9: Dependence of fitted peak centre energy on incident laser intensity for the $Si_xGe_{1-x-y}Sn_y$ samples.

V. CHARACTER OF $SI_xGE_{1-x-y}SN_y$ ALLOY VALENCE BAND STATES FROM TIGHT-BINDING SUPERCELL CALCULATIONS

In Fig. 4 of the main text we presented the calculated indirect (Ge L_{6c} and X_{5c}) and direct (Ge Γ_{7c}) character of $Si_xGe_{1-x-y}Sn_y$ alloy states lying close in energy to the conduction band (CB) edge. These calculations demonstrated the presence of strong alloy-induced band mixing in the CB, leading to significant energetic broadening of the associated L-, X- and Γ-point CB Bloch character. Here, we present the corresponding calculated character of alloy states lying close in energy to the valence band (VB) edge, demonstrating that the VB structure is much less strongly perturbed.

For the VB we take as our Ge host matrix eigenstates $|n^{(0)}\rangle$ the Γ_{8v} heavy-hole (HH) and light-hole (LH) states, and the Γ_{7v} spin-orbit split-off (SO) states. Using these states in conjunction with Eq. (2) of the main text, we compute the Ge HH/LH and SO character of the alloy VB states $|m\rangle$. We note that these VB calculations were performed using the same alloy supercells, and hence alloy eigenstates $|m\rangle$, and energy binning employed for the calculation of the CB character of the main text. The results of our VB calculations are summarised in Fig. S10, which displays the calculated Ge Γ_{8v} (HH/LH; blue) and Γ_{7v} (SO; red) character. As in Fig. 4 of the main text, the results presented in Fig. S10 have been configuration-averaged.

Beginning in panel (a), we note for reference that the HH/LH and SO states in a pure Ge supercell respectively possess 100% Γ_{8v} and Γ_{7v} character (i.e. $G_n = 1$). As the Si and Sn composition increases in panels (b) – (h) we note (i) a small reduction in energy of the HH/LH and SO VB edge energies, and (ii) an energetic broadening of the Ge Γ_{8v} and Γ_{7v} character. Here, (i) is associatfed with minimal change in the VB spin-orbit splitting energy Δ_0, while (ii) is significantly less pronounced than for the Ge L_{6c}, X_{5c} and Γ_{7c} character of the alloy CB states (cf. Fig. 4 of the main text). Indeed, we find that the energetic broadening of the Ge Γ_{8v} and Γ_{7v} character of the alloy VB states is minimal, with almost all of the calculated Ge HH/LH or SO character lying within a small energy range; note, e.g., the difference in scales on the abscissae of Fig. S10 (below) vs. Fig. 4 (main text). This indicates that the observed limited energetic broadening is driven primarily by the weak perturbation associated with the reduction in translational symmetry in the disordered alloy, rather than by a strong perturbation associated with alloy-induced hybridisation (as dominates the band structure close in energy to the CB edge).

As such, we conclude that the VB edge states in lattice-matched $Si_xGe_{1-x-y}Sn_y$/Ge alloys retain primarily Ge-like character, being minimally perturbed from those of the Ge host matrix semiconductor at the compositions of interest for photovoltaics (i.e. when the direct band gap is ~ 1 eV). From a theoretical perspective, our results then suggest overall that while the virtual crystal approximation (VCA) can likely be applied to model the $Si_xGe_{1-x-y}Sn_y$ VB structure with reasonable accuracy, beyond-VCA approaches – i.e. direct atomistic calculations or appropriately modified continuum model Hamiltonians – are required in order to quantitatively describe the nature and evolution of the CB states, and hence the alloy band gap and its optical properties.

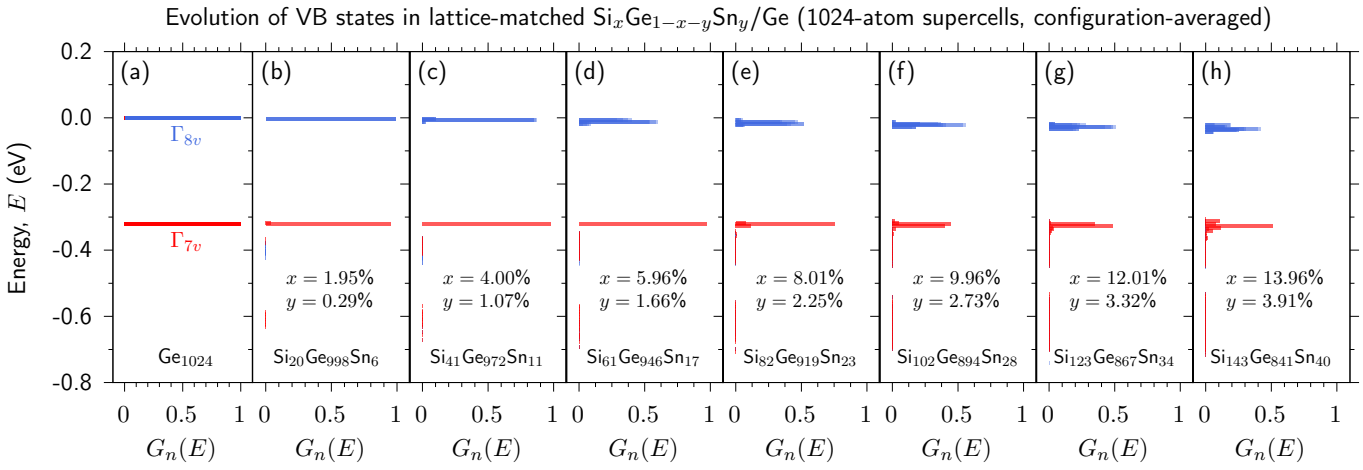


FIG. S10: Calculated evolution of the configuration-averaged Ge Γ_{8v} (blue) and Γ_{7v} (red) character of the VB states in disordered, 1024-atom $Si_xGe_{1-x-y}Sn_y$ alloy supercells lattice-matched to Ge (x:$y = 3.71$:1). Panel (a) illustrates for reference that the HH/LH (blue) and SO (red) VB edge states in pure Ge respectively possess 100% Ge Γ_{8v} and Γ_{7v} character. Substitutional incorporation of Si and Sn – panels (b)–(h) – produces minimal changes in the band structure close in energy to the VB edge. The reduction in symmetry associated with short-range alloy disorder results in inhomogeneous energetic broadening of the associated VB edge features, but much more weakly than for the alloy CB edge states. The zero of energy is taken to lie at the Ge VB edge.

* Electronic address: phoebe.pearce15@imperial.ac.uk
† Electronic address: c.broderick@umail.ucc.ie

[1] N. Kallergi, B. Roughani, J. Aubel, and S. Sundaram, Journal of Applied Physics **68**, 4656 (1990), ISSN 0021-8979, URL http://aip.scitation.org/doi/10.1063/1.346176.
[2] D. Huang, D. Mui, and H. Morkoç, Journal of Applied Physics **66**, 358 (1989), ISSN 0021-8979, URL http://aip.scitation.org/doi/10.1063/1.343882.
[3] D. Alonso-Álvarez, T. Wilson, P. Pearce, M. Führer, D. Farrell, and N. Ekins-Daukes, Journal of Computational Electronics **17**, 1099 (2018), ISSN 1569-8025, 1709.06741, URL https://doi.org/10.1007/s10825-018-1171-3http://link.springer.com/10.1007/s10825-018-1171-3.
[4] P. Pearce, S. W. Ong, A. D. Johnson, E. S. Tok, and N. J. Ekins-Daukes, J. Phys. Materials (submitted).
[5] S. Adachi, in *Physical Properties of III-V Semiconductor Compounds* (Wiley-VCH Verlag GmbH & Co. KGaA, Weinheim, FRG, 2005), vol. 783, pp. 135–192, ISBN 0471573299, URL http://doi.wiley.com/10.1002/352760281X.ch8.
[6] R. R. Lieten, K. Bustillo, T. Smets, E. Simoen, J. W. Ager, E. E. Haller, and J. P. Locquet, Physical Review B - Condensed Matter and Materials Physics **86**, 1 (2012), ISSN 10980121.
[7] F. Rathgeber, D. A. Ham, L. Mitchell, M. Lange, F. Luporini, A. T. McRae, G. T. Bercea, G. R. Markall, and P. H. Kelly, ACM Transactions on Mathematical Software (TOMS) **43**, 24 (2016), ISSN 15577295, 1501.01809, URL https://dl.acm.org/doi/abs/10.1145/2998441.
[8] W. Klingenstein and H. Schweizer, Solid State Electronics **21**, 1371 (1978), ISSN 00381101.
[9] H. van Driel, A. Elci, J. Bessey, and M. O. Scully, Solid State Communications **20**, 837 (1976), ISSN 00381098, URL https://linkinghub.elsevier.com/retrieve/pii/0038109876912862.
[10] T. Schmidt, K. Lischka, and W. Zulehner, Physical Review B **45**, 8989 (1992), ISSN 01631829.